- 1 Photoferrotrophic bacteria initiated plate tectonics in the
- 2 Neoarchean
- 3 Shengxing Zhang^{1,2,3}, Yiliang Li^{2,3,*}, Wei Leng^{1,3,*}, and Michael Gurnis⁴
- 4 Laboratory of Seismology and Physics of Earth's Interior, School of Earth and Space
- 5 Sciences, University of Science and Technology of China; Hefei, China
- 6 ²Department of Earth Sciences, the University of Hong Kong; Hong Kong, China
- ³CAS Center for Excellence in Comparative Planetology; Hefei, China
- 8 ⁴Seismological Laboratory, California Institute of Technology; Pasadena, California,
- 9 USA
- 10 *Corresponding authors: Yiliang Li (<u>viliang@hku.hk</u>), and Wei Leng

Plate tectonics distinguishes Earth from the other terrestrial planets but its

11 (wleng@ustc.edu.cn)

12 Abstract

- initiation mechanism and onset time are debated. We propose plate tectonics was initiated by deposition of magnetite-rich banded iron formations (BIFs) through biogeochemical iron cycling in Neoarchean oceans. In the photic zone of protocontinental margins, photoferrotrophic bacteria efficiently oxidized the dissolved Fe(II) and induced massive precipitation of ferric oxyhydroxide, which would rapidly react with Fe(II)-rich hydrothermal fluids from coeval vigorous volcanism in Neoarchean oceans to produce magnetite-rich BIFs. Mechanical models demonstrate that the
- 21 localization of high-density BIF deposition near proto-continents induces collapse of

- 22 the lithosphere and can initiate the earliest subduction. The peak deposition of BIFs in
- 23 2.75-2.4 Ga provides a time constraint on the inception of plate tectonics.

One Sentence Summary

- 25 The biologically induced deposition of high-density magnetite in Neoarchean oceans
- 26 initiated plate tectonics.

Main Text

24

27

28

29

30

31

32

33

34

35

36

37

38

39

40

41

42

Plate tectonics provides a powerful description of the kinematics of the solid Earth and plays a fundamental role supporting the energy, mass, and chemical cycling since its onset. However, when and how plate tectonics began has been a focus of research since its discovery (1-4). A number of mechanisms have been proposed to explain the onset of subduction and in turn, plate tectonics (5-7). Processes which localize both driving forces and lithospheric weakening are likely required. The weakening of lithosphere could occur through a combination of grain damage, grain-size reduction, thermal processes, and mineralogic change through reaction with water (8–11). External processes such as meteorite impacts have been suggested to break up the lithosphere and start subduction (5). Interior geodynamic processes such as mantle plumes (7) and the spreading of buoyant continents (6) have also been proposed as the nucleating processes of the earliest subduction. The mantle-plume model requires impingement of a hot plume head to rupture the lithosphere, while the continentspreading model emphasizes that a thick and buoyant continent is gravitationally unstable and its lateral collapse may induce subduction. These models mainly explored 43 pure geophysical processes, while overlooking the possible impact of a young

biosphere on the solid Earth which is distinctive among all the terrestrial planets.

Besides, these models did not provide a crucial time constraint for the origin of plate

tectonics.

The influence of thick sediments on subduction initiation within modern continental margin settings has long been proposed (12, 13), but the results show that the force associated with low-density (~ 2.4 g/cm³) silicate sediments cannot rupture a mature passive margin (12). Here, we argue that the banded iron formation (BIF), an early Precambrian iron-rich sedimentary rock, could lead to the requisite conditions through a combination of their high density and sequence thicknesses (Fig. S1) (14–16). The BIF deposition peaked during 2.75-2.4 Ga and distributed globally on the Neoarchean continental margins (17, 18), but their potential as the driving force of subduction initiation has not been evaluated.

The characteristics of BIF deposition

BIFs are Precambrian marine deposits composed of alternating iron-oxide and chert bands (19, 20). In the highly anoxic Archean, the oxidation of Fe(II) is widely accepted to be dominated by anaerobic photoferrotrophy. With the nutrient input from the proto-continent, photoferrotrophs thrived in the photic zone on the proto-continental margins, which have the highest contemporary primary productivity (14, 21–23). By harnessing the sunlight energy, the photoferrotrophic bacteria enzymatically oxidized Fe(II) to ferrihydrite (\sim Fe(OH)₃) and fixed CO₂ into biomass (22) (Fig. 1). Upon

diagenetic solidification, ferrihydrite dehydrated and transformed to either hematite or magnetite in BIFs, with different mineralization pathways and condensed states (15, 24). Moreover, the iron oxides in Archean BIFs are mainly magnetite, and the hematite content has gradually exceeded the magnetite content since the Proterozoic (15, 25). The hematite in BIFs was directly dehydrated from its ferrihydrite precursor, maintaining an ultrafine crystal size (3-5 nm) and a high specific surface area (~ 200 m²/g) so that it remained fluffy, similar to its oxyhydroxide precursor when settled on the seafloor (24). On the other hand, the active submarine volcanism and the released hydrothermal fluids in the Neoarchean promoted the formation of magnetite. These high Fe(II)-containing hydrothermal fluids would react with ferrihydrite on the seafloor to rapidly produce magnetite (15, 26) (Fig. 1). In contrast, magnetite nanoparticles make dense aggregation by magnetic interactions (27) (Fig. S2). The magnetite would accumulate with silica to form thick BIFs on proto-continental margins. Also, these dense BIFs typically have a density 20%-40% higher than the lithosphere due to their high iron content (14, 22). Through their negative buoyancy, such BIF-hosted continental margins eventually develop into deep sedimentary basins (Fig. 1), such as the Hamersley Basin in Western Australia (28). In addition to their dense state and high density, another important observation is the peak deposition of BIFs (2.75-2.4 Ga) (14, 18, 20). Many large BIF-hosted basins (also called Superior-type BIFs) developed in this period have been identified (18). They are found to be deposited in near-shore shelf environments and localized on

64

65

66

67

68

69

70

71

72

73

74

75

76

77

78

79

80

81

82

83

continental margin basins (17, 28), which implies a widespread distribution of BIFs on global continental margins. Moreover, the depositional scales of BIFs were large and several giant BIFs in this period (2.75-2.4 Ga) were reported, such as the Hamersley Basin in Western Australia and the Transvaal Supergroup in South Africa. These two basins alone cover an area of over 10⁵ km² and their thickness can reach kilometers (16, 28).

During the peak deposition of BIFs, a depositional rate of ~1 km/Myr has been suggested by geochronological studies (14). This is equivalent to an iron depositional rate of ~45 mol·m⁻²·yr⁻¹ for the iron-rich BIFs with Fe wt%=54.6% and ρ = 4.6 g/cm³ (14), which is close to the estimation given by recent laboratory experiments (21, 22). Assuming all the Fe(III) in BIFs is the oxidation product of photoferrotrophy and using the estimated iron-oxidation rate of the photoferrotrophic bacteria $(1-3\times10^{-11} \text{ mol·cell}^{-1}\cdot\text{yr}^{-1})$ (14, 29), a cell density of $3-9\times10^{-4}$ cells/cm³ over a 50-m-deep photic zone is adequate to sustain the abovementioned BIF depositional rates. Such a cell density should be feasible since modern observations find that the bacterial population in the photic zone is typically on the order of 10^6 cells/cm³ (14).

The high depositional rate (~1 km/Myr) implies that thick magnetite-rich BIFs would accumulate along continental margins within a few million years. The loading from these heavy sediments could be large enough to induce the rupture and subduction of the lithosphere along proto-continental margins. Based on these observations, we

propose that the peak deposition of the heavy magnetite-rich BIFs in 2.75-2.4 Ga might have initiated the earliest subduction, thus indicating the origin of plate tectonics.

Geodynamic computations of BIF-induced subduction initiation

106

107

108

109

110

111

112

113

114

115

116

117

118

119

120

121

122

123

124

125

126

We formulated 2-D thermomechanical models with viscoelastoplastic rock rheology (see Methods) to test the hypothesis that BIF deposition initiated subduction in the Neoarchean. Our reference model (Fig. 2) consists of a 100-km-thick protocontinental plate (left side, 1100 km wide) and a 100-km-thick oceanic plate (right side, 2100 km wide). Presumably, crustal thickness variations before plate tectonics would have been gradual as they would have partially relaxed over millions of years. We assumed that before plate tectonics that there were regions of proto-continent composed of crust like tonalite–trondhjemite–granodiorite rocks with a density of $\sim 2.9 \text{ g/cm}^3$ (30). Consequently, a transition (from x=1000 km to x=1100 km) between proto-continent and an oceanic domain is set (Fig. 2A). The crustal thickness of the proto-continent and the oceanic plate is 30 km and 15 km, respectively. A 40-km-thick "sticky air" layer above the lithosphere approximates the free surface (31). The initial temperature field of the proto-continental and oceanic lithosphere is linearly distributed between 0°C and 1550°C, while the sublithospheric temperature is homogeneous (1550 °C) and 200 °C higher than the modern value (6) (Fig. 2A). The width of the BIF-depositional area d_0 beneath the proto-continental margin is nominally set to 250 km (i.e., from x=1100 km to x=1350 km in Fig. 2A), which is comparable to the width of modern mature passive margins (12). BIF material is deposited on proto-continental margins at specified

depositional rates (see Methods for details) (Fig. 2). Modelled BIFs are localized on the proto-continental margin through a terrestrial nutrient input needed by the photoferrotrophic bacteria. We established a 1-D ocean-mixing model (see Methods) to determine the spatial distribution of the depositional rate $v_d(x)$ (Fig. 2G). With a nonuniform depositional rate, a horizontally-averaged value v_{ave} is used when comparing models. The yield stress of the marine sediments is believed to be low and we use the value determined from previous studies (32) in the model (Table. S1). For the reference model (Fig. 2), enough BIF sediments accumulate within ~9 Myrs to rupture the lithosphere when the peak BIF depositional rate is maintained at 1 km/Myr. Initially, the sedimentary loading is limited to moderate plate deflections (Fig. 2B). However, as the sediments are weak, they flow horizontally, increasing the downward deflection of the lithosphere, which in turn leads to more localization of the high-density BIFs. The thickness of the sediments rapidly evolves away from the profile imposed by the ocean-mixing model (Fig. 2G) to one with a more Gaussian shape (Fig. 2B) and eventually one which is even more localized (Fig. 2C). As the thickness of BIF sediments increases, the load eventually exceeds the yield strength of the lithosphere and the margin collapses (Fig. 2C). After several million years, a retreating subduction slab starts at the position of plate rupture (Fig. 2D). In the computations, when the lithosphere breaks and sinks into the mantle, BIF deposition shuts down and the horizontal-average BIF thickness at this time is recorded as the critical thickness (see

127

128

129

130

131

132

133

134

135

136

137

138

139

140

141

142

143

144

145

Methods for details), which represents the minimum BIF thickness required to break the lithosphere.

149

150

151

152

153

154

155

156

157

158

159

160

161

162

163

164

165

166

167

Compared with the reference model (Fig.2), thicker BIF sediment is required to induce subduction when either the yield stress or the thickness of lithosphere is increased (Figs. 3A-3B). When the maximum yield stress of the lithosphere increased from 150 MPa to 600 MPa, the critical thickness of the BIF to rupture a 100-km-thick lithosphere varies from ~5 km to ~12 km. (Fig. 3A). When the yield stress of the lithosphere is 300 MPa as recently estimated (6) and the lithospheric thickness increased from 75 km to 125 km, the critical thickness changes from ~5 km to ~11 km. (Fig. 3B). The thickness of the proto-continental crust can significantly influence the buoyancy and strength of the lithosphere, but its value before plate tectonics is poorly constrained. We change the thickness from 20 km to 40 km and the corresponding critical thickness of BIFs varies from ~12 km to ~5 km (Fig. 3C). Different densities of BIF from 4.6 g/cm³ (iron-rich BIF, Fe wt% \approx 55%) to 3.8 g/cm³ (Fe wt% \approx 35%) are tested, and the related critical thickness varies from ~9 km to ~14 km (Fig. 3D). The outcomes may also be affected by the degree to which deposition is localized, the sharpness of the ocean-continent transition, the sediment strength, and the time interval of deposition. When we changed d_0 (depositional scale) from 150 km to 300 km, the average depositional rate v_{ave} from 0.2 km/Myr to 2 km/Myr, the width of the transitional area between proto-continent and ocean from 0 km to 100 km, the friction coefficient of BIF from 0.0 to 0.1, and the time interval to deposit BIFs from 0.2 Myr

to 1 Myr, computations show that the critical thickness of BIFs is not substantially influenced (Figs. S3A-E).

On modern passive margins, the thickness of the low-density silicate sediments can reach 15-20 km (Fig. S4A). However, with the deposition of BIFs, such a thickness is sufficient to induce subduction. In fact, the negative buoyancy of BIFs would drive it to subside continuously and deepen the basin (28), so the upper bound of sedimentary thickness should be higher. Based on the computations and observed characteristics of BIFs in the Neoarchean (including its high density and depositional rate), magnetiterich BIFs can trigger subduction over only a few million years (~ 10 Myrs).

The biological-induced origin of plate tectonics

The computations show that subduction initiation induced by magnetite-rich BIFs is physically plausible, and with a distinctive biomineralization genesis for BIFs implies a biologically induced origin of plate tectonics. As one of the earliest energy metabolisms on Earth, the prosperity of photoferrotrophy presets the global tectonic environments. The photoferrotrophic bacteria used the Fe(II) source in the anoxic seawater and efficiently metabolized it to acquire the necessary energy. Their thriving in the Neoarchean (Fig. 4A) led to the massive deposition of ferrihydrite on the protocontinental margins. Meanwhile, vigorous submarine volcanism in the Neoarchean (*33*) should have significantly increased the supply of hydrothermal Fe(II) to the photic zone, which has reacted with the ferrihydrite directly to make dense magnetite deposition on the seafloor at the proto-continental margins (*15*, *26*). The synchronous appearance of

the anoxic oceanic environment (34), the high Fe(II)-oxidizing rate from thriving photoferrotrophs (14), and the abundant hydrothermal Fe(II) alternations in the Neoarchean (33) satisfied the conditions to deposit massive magnetite-rich BIFs rapidly (15, 26) (Fig. 4B). We propose that these dense and high-density sediments on the protocontinental margins broke the lithosphere, induced the earliest subduction, and initiated plate tectonics.

The BIFs that subducted presumably would have sunk into the deeper mantle; the transport of BIFs into the lower mantle has previously been suggested as a mechanism to form the ultralow-velocity zones (ULVZs) at the core-mantle boundary (35). Interestingly, ULVZs are generally hundreds of kilometers wide, tens of kilometers high, and thought to be composed of high density, Fe-rich material (36), not unlike the BIF sedimentary packages required to trigger subduction initiation.

However, the distinctive biogeochemical formation of magnetite gradually shut down after the Neoarchean. The oxidation of the ocean since the early Paleoproterozoic (Fig. 4C) has significantly depressed the dissolved Fe(II) in the seawater, reducing the contribution of photoferrotrophy to primary production and ferric oxide deposition (15). After the Great Oxidation Event (GOE) (Fig. 4C), the emerging oxygenic photosynthesis gradually surpassed the anaerobic photoferrotrophy (Fig. 4A) so that the BIF deposition was significantly decreased (18) (Fig. 4B) and contained less magnetite (15, 25). On modern continental margins, the marine photic zone overlaps subduction zones, a similar scene we propose at the onset time of the global plate tectonics in the

Neoarchean (Fig. S4). Following the Neoarchean, the low-density silicate deposits replaced the heavy BIFs, and sediment-induced subduction initiation shut down by which time new subduction zones could continuously formed by mechanisms now seen in the plate tectonic system (37).

The onset time of plate tectonics

210

211

212

213

214

215

216

217

218

219

220

221

222

223

224

225

226

227

228

229

230

Our model implies a timing for the start of global plate tectonics. Despite longstanding discussion on this timing (1, 3, 4), most studies accept that the onset of plate tectonics is coeval with the onset of earliest subduction (6, 38). Based on our model, the earliest subduction started on global continental margins and was triggered by the rapid BIF deposition during 2.75-2.4 Ga, which is well supported by many contemporary plate-tectonic indicators and geological events. During the transition from the Neoarchean to Paleoproterozoic, volcanism recorded by large igneous provinces (LIPs) gradually shifted from submarine to subaerial (34) (Fig. 4D). Since submarine volcanism is more reductive than subaerial volcanism (34), the preponderance of submarine LIPs in the Archean is consistent with the anoxic environment at that time and the related submarine hydrothermal alteration could provide the Fe(II) for the rapid mineralization of magnetite during peak BIF deposition (15). Once plate tectonics began, the frequent subduction of the oceanic lithosphere would make submarine LIPs preferentially destroyed and short-lived (34). Therefore, the decrease of submarine-volcano proportion since the Neoarchean-Paleoproterozoic transition (Fig. 4D) probably corresponds to the time when BIF first induced the

subduction of the oceanic plates. The existence of subduction is supported by the identification of the earliest paired metamorphic units (2.54-2.50 Ga) in the Neoarchean granite-greenstone belt (39) (Fig. 4E). With the establishment of subduction zones, large-scale horizontal plate movement would start and is consistent with recent palaeomagnetic reconstructions suggesting such movements (> 5000 km) between cratonic blocks already existed by ca. 2.7-2.4 Ga (1) (Fig. 4E). The crustalgrowth peaked in the Neoarchean (2.7-2.5 Ga) (40) (Fig. 4E) also supports our scenario. Arc magmatism resulting from the earliest subduction would greatly promote the production of the continental crust, which provides a reasonable interpretation for the rapid crustal growth in this period (40). Convergent boundaries such as subduction zones are not the only proxy of plate tectonics, as divergent boundary records such as mid-ocean ridges (MORs) are proxies as well. The appearance of the oldest divergent-boundary records in the Neoarchean (1, 4) (Fig. 4E) supports the inferred start of plate tectonics. Such records can be traced back to 2.75-2.5 Ga in several Archean cratons (1). The appearance of nascent MORs means that more Fe(II)-rich fluids would be available for magnetite mineralization. Because of the higher elevation of these oceanic ridges compared with oceanic basins, the released hydrothermal Fe(II) fluids would reach the upper ocean layer close to the BIF-deposition depth more easily (15), facilitating the rapid and massive deposition of magnetite-rich BIFs.

231

232

233

234

235

236

237

238

239

240

241

242

243

244

245

246

247

248

249

In this model of plate tectonics initiation, we find the extraordinary role of photoferrotrophic bacteria on early Earth. They effectively oxidize the dissolved ferrous iron and aggregate the resulting ferric oxides onto proto-continental margins, which were turned to the dense magnetite by further reaction of Fe(II) from the submarine hydrothermal fluids. These dense and high-density banded iron sediments could break the proto-continental margins to start subduction and kick-started plate tectonics. Their peak deposition in 2.75-2.4 Ga constrains the time plate tectonics started. This unique biogeochemical cycle with the biomineralization of amorphous ferrihydrite and the magnetization by the addition of hydrothermal Fe(II) fluids could only happen on Earth and only once during this period. The model implies that prosperous photoferrotrophy in the Neoarchean is the reason why Earth is the only planet with plate tectonics. In this sense, life has played an even more important role in uniquely shifting the tectonic style of Earth to a plate tectonic system.

265 Figures

267

268

269

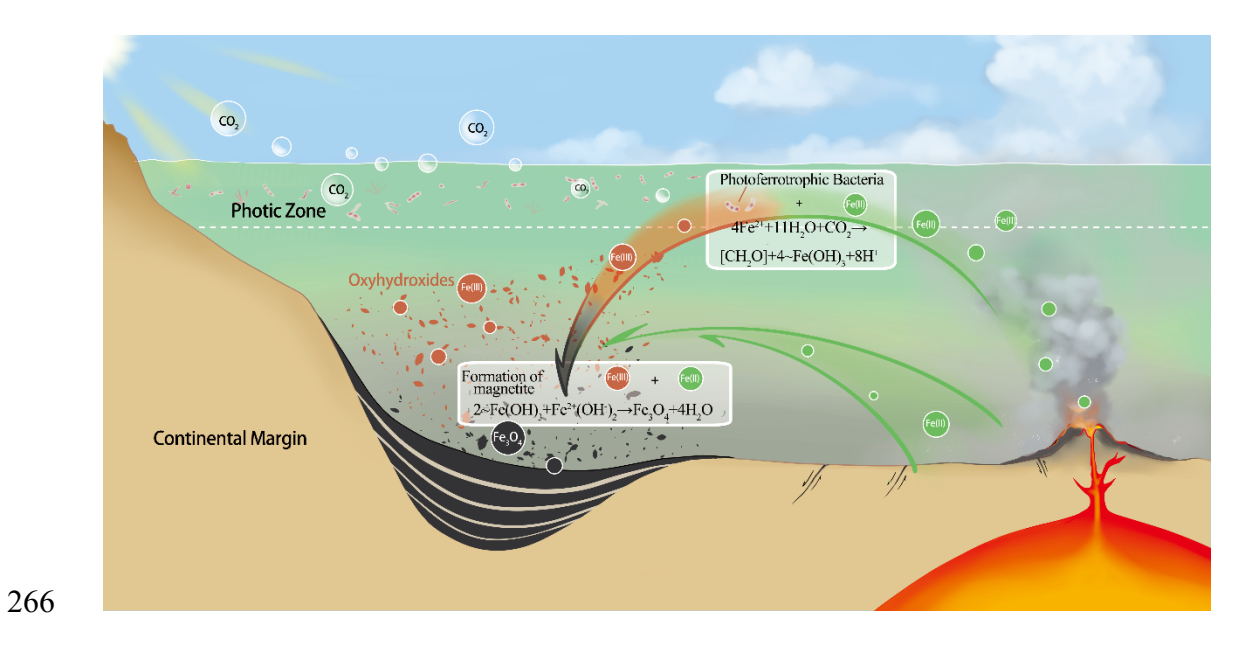


Figure 1 | Schematic diagram showing the formation of magnetite-rich BIFs on the Neoarchean continental margins facilitated by the photoferrotrophic bacteria.

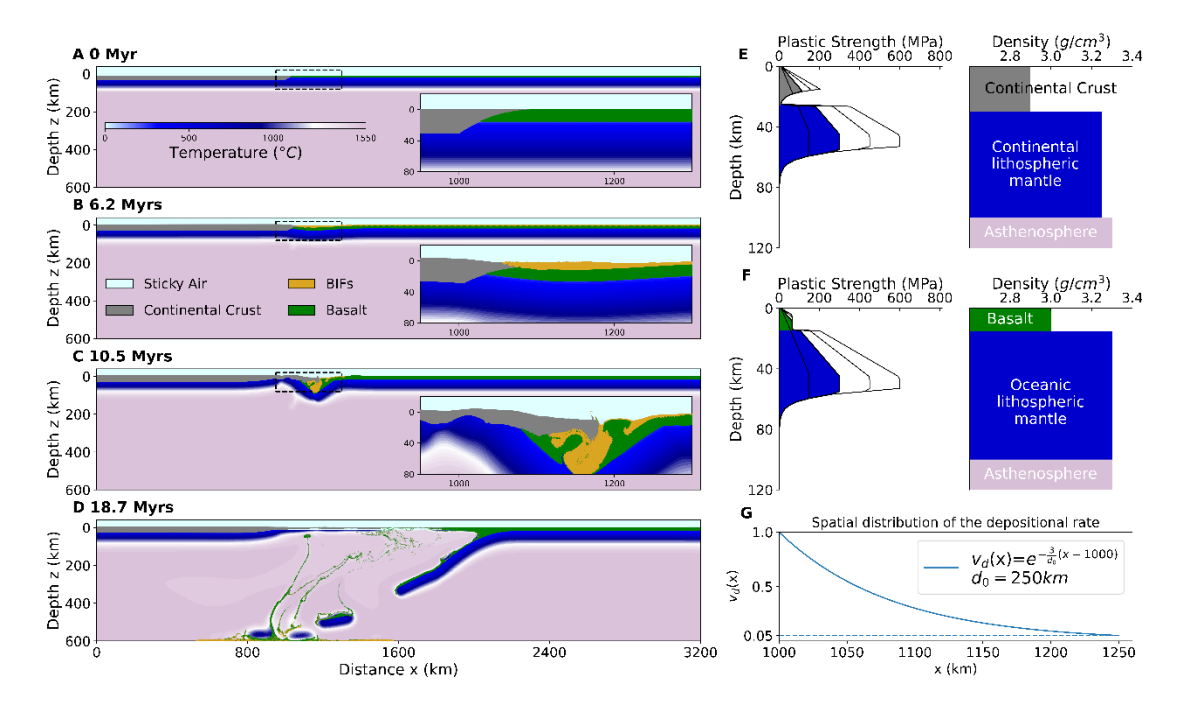


Figure 2 | Computation of the subduction initiation process triggered by magnetite-rich BIFs. A. The initial settings of the reference model. B-D. The evolution snapshots in 7.2, 9.9, and 19.5 Myrs. The enlarged views of the depositional area (dashed box) in (A-C) are shown in the inset figures on the right. The crustal particles are superimposed on the original temperature field to distinguish the proto-continent (grey) from the ocean (green). BIF sediments are denoted in yellow. E-F. Plastic-strength and density settings of the proto-continental plate (E) and the oceanic plate (F) in the reference model. The density of BIFs in the reference model is set to 4.6 g/cm³. G. The spatial distribution of the normalized depositional rate.

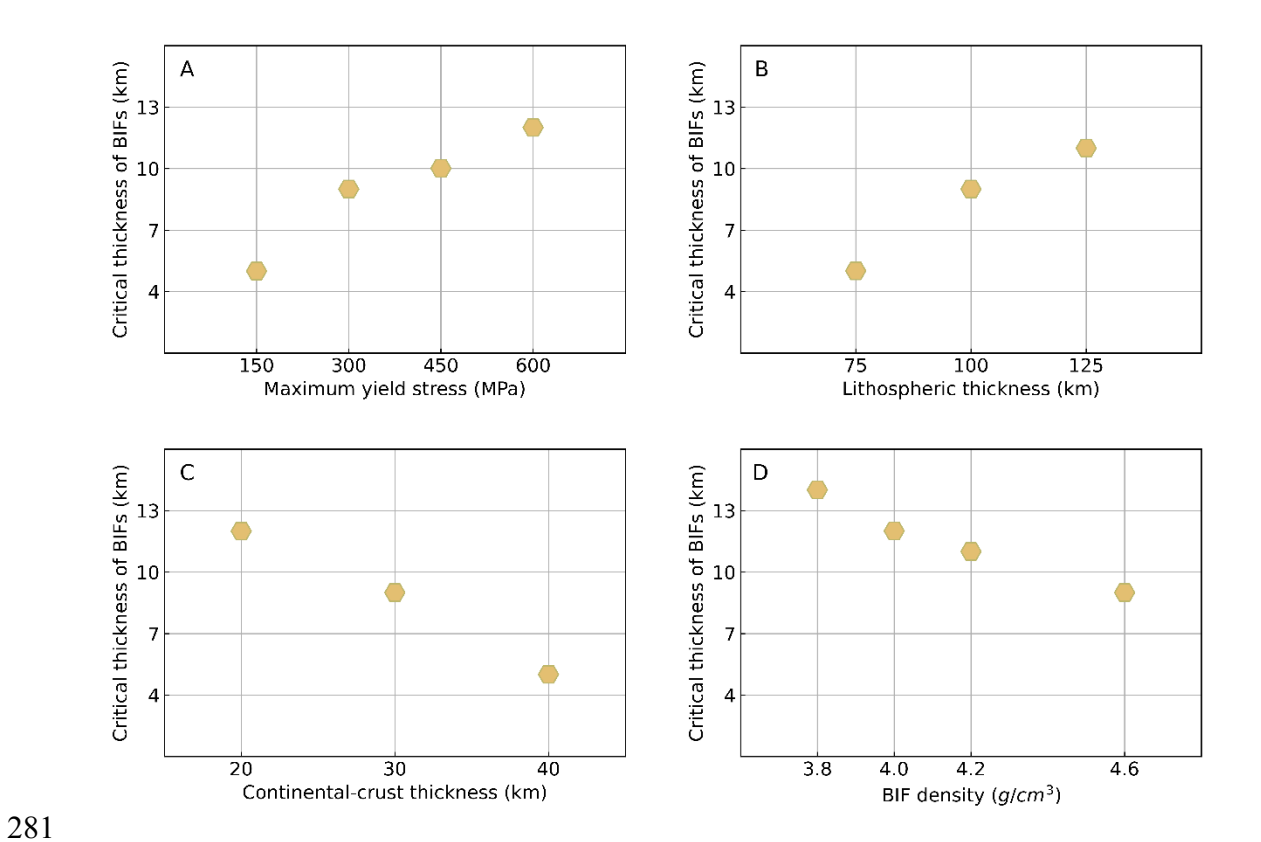


Figure 3. Critical thickness of BIFs required for subduction initiation with different mechanical and sediment parameters: A. Yield stress of the lithosphere. B. Lithospheric thickness. C. Thickness of proto-continental crust. D. Aggregate BIF density.

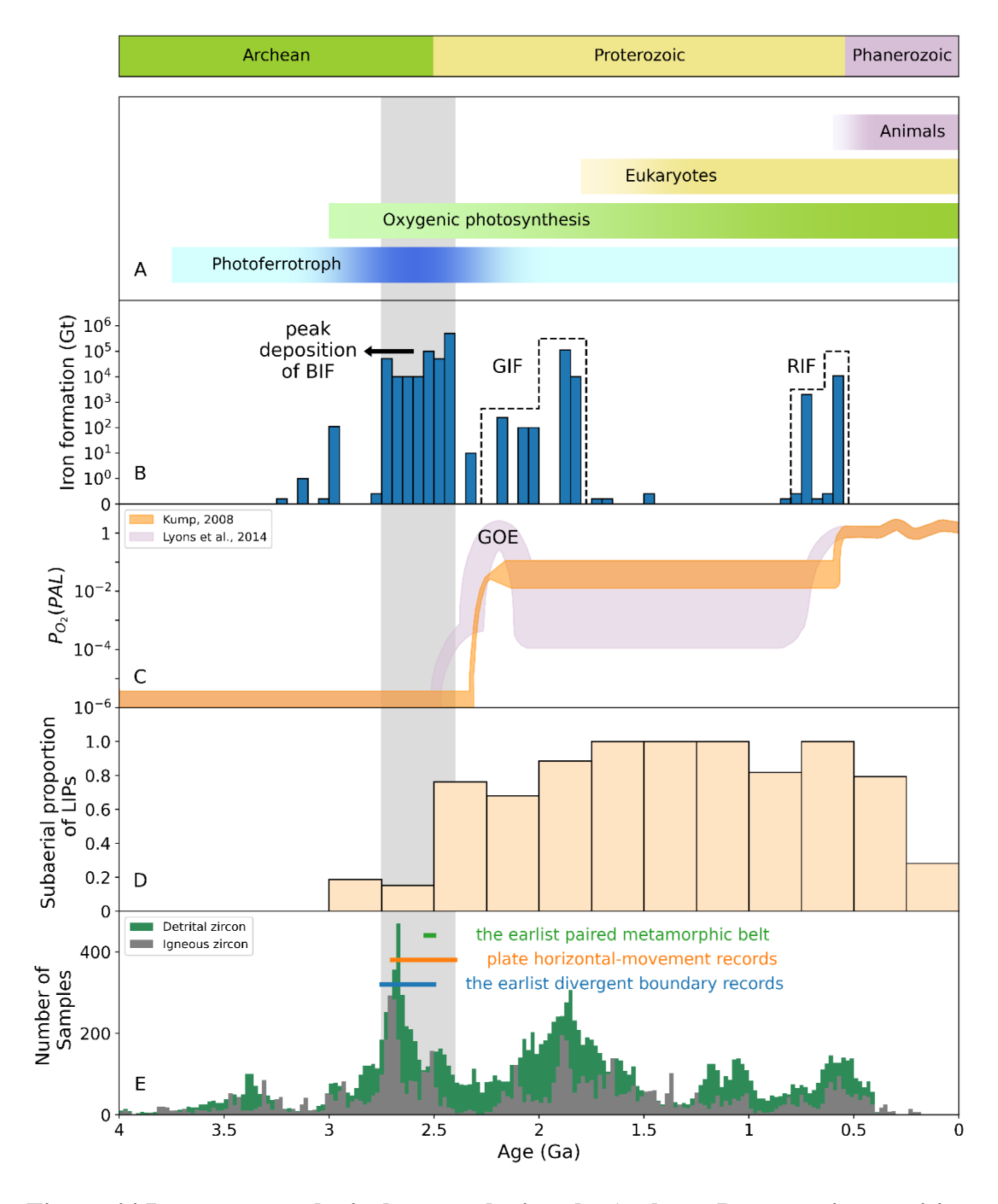


Figure 4 | **Important geological events during the Archean-Proterozoic transition period. A.** The evolutionary timeline of the biosphere (*41*). **B.** Frequency histogram of the iron formation (IF) with 50-Myr-wide bars (*18*). Most IFs before 2.4 Ga belong to BIF (*18*). The sediments in 2.3–0.8 Ga and 0.8-0.56 Ga are dominated by the granular iron formation (GIF) and the Rapitan-type iron formation (RIF), respectively (*18*). **C.** Evolution models of atmospheric oxygen content suggested by ref. (*42*) (purple) and

ref. (43) (orange). P_{O_2} : atmospheric partial pressure of oxygen relative to the present atmospheric level (PAL); GOE: Great Oxygenation Event. **D.** Secular variation in proportion of subaerial LIPs (34). The total large igneous provinces (LIPs) are divided into two types, the subaerial LIPs and the submarine ones. **E.** Distribution of the detrital and the igneous zircons reported by ref. (40) and other plate-tectonic indicators in the Neoarchean.

References and Notes

- 302 1. P. A. Cawood, C. J. Hawkesworth, S. A. Pisarevsky, B. Dhuime, F. A.
- Capitanio, O. Nebel, Geological archive of the onset of plate tectonics. *Philos*.
- 304 Trans. R. Soc. A Math. Phys. Eng. Sci. **376**, 20170405 (2018).
- 305 2. R. J. Stern, The evolution of plate tectonics. *Philos. Trans. R. Soc. A Math.*
- 306 Phys. Eng. Sci. 376, 20170406 (2018).
- 307 3. J. Korenaga, Initiation and Evolution of Plate Tectonics on Earth: Theories and
- 308 Observations. *Annu. Rev. Earth Planet. Sci.* **41**, 117–151 (2013).
- 309 4. K. C. Condie, A. Kröner, "When did plate tectonics begin? Evidence from the
- geologic record" in Special Paper 440: When Did Plate Tectonics Begin on
- 311 Planet Earth? (Geological Society of America, 2008;
- https://pubs.geoscienceworld.org/books/book/594/chapter/3804524/), vol. 440,
- 313 pp. 281–294.
- 5. V. L. Hansen, Subduction origin on early Earth: A hypothesis. *Geology*. **35**,
- 315 1059 (2007).
- 316 6. P. F. Rey, N. Coltice, N. Flament, Spreading continents kick-started plate
- 317 tectonics. *Nature*. **513**, 405–408 (2014).
- 7. T. V. Gerya, R. J. Stern, M. Baes, S. V. Sobolev, S. A. Whattam, Plate
- tectonics on the Earth triggered by plume-induced subduction initiation.
- 320 *Nature.* **527**, 221–225 (2015).

- 321 8. J. Escartín, G. Hirth, B. Evans, Strength of slightly serpentinized peridotites:
- 322 Implications for the tectonics of oceanic lithosphere. *Geology.* **29**, 1023 (2001).
- 323 9. J. P. Poirier, Shear localization and shear instability in materials in the ductile
- 324 field. J. Struct. Geol. 2, 135–142 (1980).
- 325 10. M. Thielmann, B. J. P. Kaus, Shear heating induced lithospheric-scale
- localization: Does it result in subduction? Earth Planet. Sci. Lett. **359–360**, 1–
- 327 13 (2012).
- 328 11. E. Mulyukova, D. Bercovici, Formation of lithospheric shear zones: Effect of
- temperature on two-phase grain damage. *Phys. Earth Planet. Inter.* **270**, 195–
- 330 212 (2017).
- 331 12. S. A. P. L. Cloetingh, M. J. R. Wortel, N. J. Vlaar, Evolution of passive
- continental margins and initiation of subduction zones. *Nature*. **297**, 139–142
- 333 (1982).
- 334 13. S. G. Erickson, Sedimentary loading, lithospheric flexure, and subduction
- initiation at passive margins. *Geology*. **21**, 125 (1993).
- 336 14. K. O. Konhauser, T. Hamade, R. Raiswell, R. C. Morris, F. Grant Ferris, G.
- 337 Southam, D. E. Canfield, Could bacteria have formed the Precambrian banded
- iron formations? *Geology*. **30**, 1079 (2002).
- 339 15. Y.-L. Li, K. O. Konhauser, M. Zhai, The formation of magnetite in the early
- 340 Archean oceans. Earth Planet. Sci. Lett. 466, 103–114 (2017).

- 16. L. J. Robbins, S. P. Funk, S. L. Flynn, T. J. Warchola, Z. Li, S. V. Lalonde, B.
- J. Rostron, A. J. B. Smith, N. J. Beukes, M. O. de Kock, L. M. Heaman, D. S.
- Alessi, K. O. Konhauser, Hydrogeological constraints on the formation of
- Palaeoproterozoic banded iron formations. *Nat. Geosci.* **12**, 558–563 (2019).
- 345 17. K. O. Konhauser, N. J. Planavsky, D. S. Hardisty, L. J. Robbins, T. J.
- Warchola, R. Haugaard, S. V. Lalonde, C. A. Partin, P. B. H. Oonk, H. Tsikos,
- T. W. Lyons, A. Bekker, C. M. Johnson, Iron formations: A global record of
- Neoarchaean to Palaeoproterozoic environmental history. *Earth-Science Rev.*
- **172**, 140–177 (2017).
- 350 18. A. Bekker, J. F. Slack, N. Planavsky, B. Krapez, A. Hofmann, K. O.
- 351 Konhauser, O. J. Rouxel, Iron Formation: The Sedimentary Product of a
- Complex Interplay among Mantle, Tectonic, Oceanic, and Biospheric
- 353 Processes. Econ. Geol. 105, 467–508 (2010).
- 354 19. Y.-L. Li, Micro- and nanobands in late Archean and Palaeoproterozoic banded-
- iron formations as possible mineral records of annual and diurnal depositions.
- 356 Earth Planet. Sci. Lett. **391**, 160–170 (2014).
- 20. C. Klein, Some Precambrian banded iron-formations (BIFs) from around the
- world: Their age, geologic setting, mineralogy, metamorphism, geochemistry,
- and origins. Am. Mineral. **90**, 1473–1499 (2005).

- 360 21. A. Kappler, C. Pasquero, K. O. Konhauser, D. K. Newman, Deposition of
- banded iron formations by anoxygenic phototrophic Fe(II)-oxidizing bacteria.
- 362 Geology. **33**, 865 (2005).
- 363 22. K. J. Thompson, P. A. Kenward, K. W. Bauer, T. Warchola, T. Gauger, R.
- Martinez, R. L. Simister, C. C. Michiels, M. Llirós, C. T. Reinhard, A.
- Kappler, K. O. Konhauser, S. A. Crowe, Photoferrotrophy, deposition of
- banded iron formations, and methane production in Archean oceans. Sci. Adv.
- **5**, eaav2869 (2019).
- 368 23. R. Wollast, "Continental Margins Review of Geochemical Settings" in
- 369 Ocean Margin Systems (Springer Berlin Heidelberg, Berlin, Heidelberg, 2002;
- 370 http://link.springer.com/10.1007/978-3-662-05127-6 2), pp. 15–31.
- 371 24. S. Sun, K. O. Konhauser, A. Kappler, Y.-L. Li, Primary hematite in
- Neoarchean to Paleoproterozoic oceans. *Geol. Soc. Am. Bull.* **127**, 850–861
- 373 (2015).
- 374 25. H. L. James, "Chapter 11 Precambrian Iron-Formations: Nature, Origin, and
- 375 Mineralogic Evolution from Sedimentation to Metamorphism" in *Orthodontic*
- 376 Treatment of Class III Malocclusion (1992;
- https://linkinghub.elsevier.com/retrieve/pii/S0070457108705739), vol. 1990,
- 378 pp. 543–589.

- 379 26. I. Halevy, M. Alesker, E. M. Schuster, R. Popovitz-Biro, Y. Feldman, A key
- role for green rust in the Precambrian oceans and the genesis of iron
- 381 formations. *Nat. Geosci.* **10**, 135–139 (2017).
- 382 27. R. L. Rebodos, P. J. Vikesland, Effects of oxidation on the magnetization of
- 383 nanoparticulate magnetite. *Langmuir*. **26**, 16745–16753 (2010).
- 384 28. A. F. Trendall, The hamersley basin. *Dev. Precambrian Geol.* **6**, 69–129
- 385 (1983).
- 386 29. M. Maisch, U. Lueder, K. Laufer, C. Scholze, A. Kappler, C. Schmidt,
- 387 Contribution of Microaerophilic Iron(II)-Oxidizers to Iron(III) Mineral
- 388 Formation. *Environ. Sci. Technol.* **53**, 8197–8204 (2019).
- 389 30. J. D. Merriman, A. G. Whittington, A. M. Hofmeister, P. I. Nabelek, K. Benn,
- Thermal transport properties of major Archean rock types to high temperature
- and implications for cratonic geotherms. *Precambrian Res.* **233**, 358–372
- 392 (2013).
- 393 31. F. Crameri, H. Schmeling, G. J. Golabek, T. Duretz, R. Orendt, S. J. H. Buiter,
- D. A. May, B. J. P. Kaus, T. V. Gerya, P. J. Tackley, A comparison of
- numerical surface topography calculations in geodynamic modelling: an
- evaluation of the 'sticky air' method. Geophys. J. Int. 189, 38–54 (2012).
- 397 32. D. M. Davis, R. von Huene, Inferences on sediment strength and fault friction
- from structures at the Aleutian Trench. *Geology*. **15**, 517 (1987).

- 399 33. A. E. Isley, D. H. Abbott, Plume-related mafic volcanism and the deposition of
- banded iron formation. J. Geophys. Res. Solid Earth. 104, 15461–15477
- 401 (1999).
- 402 34. L. R. Kump, M. E. Barley, Increased subaerial volcanism and the rise of
- 403 atmospheric oxygen 2.5 billion years ago. *Nature*. **448**, 1033–1036 (2007).
- 404 35. D. P. Dobson, J. P. Brodholt, Subducted banded iron formations as a source of
- 405 ultralow-velocity zones at the core–mantle boundary. *Nature*. **434**, 371–374
- 406 (2005).
- 407 36. D. J. Bower, J. K. Wicks, M. Gurnis, J. M. Jackson, A geodynamic and mineral
- 408 physics model of a solid-state ultralow-velocity zone. Earth Planet. Sci. Lett.
- **303**, 193–202 (2011).
- 410 37. M. Gurnis, "An evolutionary perspective on subduction initiation" in *Dynamics*
- 411 of Plate Tectonics and Mantle Convection, J. C. Duarte, Ed. (Elsevier, 2022).
- 412 38. T. V. Gerya, R. J. Stern, M. Baes, S. V. Sobolev, S. A. Whattam, Plate
- 413 tectonics on the Earth triggered by plume-induced subduction initiation.
- 414 *Nature.* **527**, 221–225 (2015).
- 415 39. B. Huang, T. M. Kusky, T. E. Johnson, S. A. Wilde, L. Wang, A. Polat, D. Fu,
- Paired metamorphism in the Neoarchean: A record of accretionary-to-
- 417 collisional orogenesis in the North China Craton. Earth Planet. Sci. Lett. 543,
- 418 116355 (2020).

- 419 40. K. C. Condie, E. Belousova, W. L. Griffin, K. N. Sircombe, Granitoid events in
- space and time: Constraints from igneous and detrital zircon age spectra.
- 421 *Gondwana Res.* **15**, 228–242 (2009).
- 422 41. A. H. Knoll, M. A. Nowak, The timetable of evolution. Sci. Adv. 3, 1–14
- 423 (2017).
- 424 42. L. R. Kump, The rise of atmospheric oxygen. *Nature*. **451**, 277–278 (2008).
- 425 43. T. W. Lyons, C. T. Reinhard, N. J. Planavsky, The rise of oxygen in Earth's
- 426 early ocean and atmosphere. *Nature*. **506**, 307–315 (2014).
- 427 44. L. Moresi, F. Dufour, H.-B. Mühlhaus, A Lagrangian integration point finite
- element method for large deformation modeling of viscoelastic geomaterials. J.
- 429 *Comput. Phys.* **184**, 476–497 (2003).
- 430 45. C. O'Neill, L. Moresi, D. Müller, R. Albert, F. Dufour, Ellipsis 3D: A particle-
- in-cell finite-element hybrid code for modelling mantle convection and
- lithospheric deformation. *Comput. Geosci.* **32**, 1769–1779 (2006).
- 433 46. S. -i. Karato, P. Wu, Rheology of the Upper Mantle: A Synthesis. *Science*
- 434 *(80-.).* **260**, 771–778 (1993).
- 435 47. G. Ranalli, Rheology of the Earth 2nd edn (Springer Science & Business
- 436 Media, 1995).
- 437 48. Z. H. Li, T. Gerya, J. A. D. Connolly, Variability of subducting slab
- 438 morphologies in the mantle transition zone: Insight from petrological-
- thermomechanical modeling. *Earth-Science Rev.* **196**, 102874 (2019).

440 K. K. McCall, C. E. Martin, Chlorophyll Concentrations and Photosynthesis in 49. Three Forest Understory Mosses in Northeastern Kansas. Bryologist. 94, 25 441 442 (1991).443 444 Acknowledgements 445 Fundings: S.Z., Y.L., and W.L. acknowledge financial support from the Strategic Priority Research Program of Chinese Academy of Sciences (XDB41000000). M.G. 446 was supported by NSF OCE-2049086. Author contributions: Y.L. and W.L. 447 448 developed the concept of the project and designed models. S.Z. performed the calculations. S.Z., Y.L., W. L. and M.G. did the analysis and wrote the paper. 449 450 Competing interests: The authors declare no competing interests. Data and materials 451 availability: The code Ellipsis is available at CIG (www.geodynamics.org/cig). The thickness data is from www.ngdc.noaa.gov/mgg/sedthick. The 452 sedimentary chlorophyll-a data is from NASA OceanColor (www.oceancolor.gsfc.nasa.gov). The 453 454 data of subduction boundaries is from GPlates (www.gplates.org). 455 456 **List of Supplementary Materials** 457 Materials and Methods Figs. S1 to S4 458 Table S1 459 References 460

Materials and Methods

463 Governing equations

- The calculation in our thermomechanical model with two-dimensional Cartesian geometry is performed using the Ellipsis software (44, 45), which combines the finiteelement method with a particle-in-cell method to solve the conservation equations of
- 467 mass, momentum, and energy:

$$\frac{\partial v_i}{\partial x_i} = 0,\tag{1}$$

469
$$\frac{\partial \tau_{ij}}{\partial x_j} - \frac{\partial P}{\partial x_i} = \rho g_i \ (i, j = 1, 2), \tag{2}$$

$$\rho C_p \frac{DT}{Dt} = \frac{\partial}{\partial x_i} \left(k \frac{\partial T}{\partial x_j} \right) + H, \tag{3}$$

- 471 where v_i represents the velocity in the x_i direction, τ_{ij} is the deviatoric stress tensor,
- 472 P is the pressure, ρ is the density, g_i is the gravitational acceleration in the x_i
- direction, T is the temperature, C_p is the isobaric heat capacity, k (= $\kappa \rho C_p$ where
- κ denotes the thermal diffusivity) is the thermal conductivity, and $\frac{D}{Dt}$ represents the
- 475 material derivative. H is the heat generation, including radioactive heating H_r , shear
- heating H_s , and adiabatic heating H_a (i.e., $H = H_r + H_s + H_a$).
- The density is temperature-dependent:

478
$$\rho = \rho_0 [1 - \alpha (T - T_{r0})], \tag{4}$$

- 479 where ρ_0 is the reference density, α is the thermal expansion coefficient, and
- 480 T_{r0} (273 K) is the reference temperature for the density.

481 Material description

An incompressible Maxwell-rheological model is adopted to reflect viscoelastic

483 behavior:

484
$$\dot{\varepsilon}_{ij} = \frac{1}{2K_e} \dot{S}_{ij} + \frac{1}{2\eta} S_{ij}, \tag{5}$$

- 485 where $\dot{\varepsilon}_{ij}$ is the strain rate tensor, S_{ij} is the deviatoric part of the stress tensor, \dot{S}_{ij} is
- 486 the Jaumann corotational rate of S_{ij} , K_e is the shear modulus for elasticity, and η is
- 487 the viscosity.
- Both dislocation creep (η_{dl}) and diffusion creep (η_{df}) (46) contribute to the
- 489 viscosity:

490
$$\eta_{dl/df} = \eta_0 \left(\frac{\dot{\varepsilon}_{II}}{\dot{\varepsilon}_0}\right)^{\frac{1}{n-1}} exp\left[\frac{E + PV}{nR(T - T_0)}\right],\tag{6}$$

- 491 where η_0 is the reference viscosity, $\dot{\varepsilon}_{II}$ is the second invariant of the deviatoric strain
- 492 rate tensor, $\dot{\varepsilon}_0$ (= $10^{-15} \, s^{-1}$) is the reference strain rate, n is the strain exponent, E
- 493 is the activation energy, V is the activation volume, $R = 8.31 \, J \cdot mol^{-1}$ is the gas
- 494 constant, T is the temperature, T_0 (= 1823 K) is the reference temperature for the
- 495 viscosity, and *P* is the pressure.
- 496 For crustal rocks, only dislocation creep contributes (47):

$$\eta_{crust} = \eta_{dl} \tag{7}$$

For the mantle, both dislocation creep and diffusion creep (46) are considered:

$$\eta_{mantle} = \left(\frac{1}{\eta_{dl}} + \frac{1}{\eta_{df}}\right)^{-1} \tag{8}$$

For simplicity, we use the parameters of quartzite (48) to calculate the viscosity of

all crustal rocks and use the parameters of olivine (48) for the mantle viscosity.

Viscosity is truncated to ensure convergence of eq.1 and 2, which requires η to lie between η_{min} (10¹⁹ $Pa \cdot s$) and η_{max} (10²⁴ $Pa \cdot s$).

The plastic behavior is described by the Drucker-Prager yield criterion:

$$\tau_{yield} = \min(\mu P + C, \tau_{max}), \tag{9}$$

and a linear strain-weakening plastic model:

$$\mu = \mu_0 \left[1 - \min(1, \frac{\varepsilon_p}{\varepsilon_f}) \right], \tag{10}$$

$$C = C_f + \left(C_0 - C_f\right) \left[1 - \min(1, \frac{\varepsilon_p}{\varepsilon_f})\right], \tag{11}$$

where τ_{yield} , τ_{max} , μ , P, C, μ_0 , C_0 , C_f , ε_p , and ε_f represent yield stress, upper bound of the yield stress, friction coefficient, total pressure, cohesion, initial friction coefficient, initial cohesion, minimum cohesion, integrated plastic strain, and reference plastic strain (set to 0.3), respectively.

Model settings

The size of the computational domain (Fig. 2A) is 600 km in depth and 3200 km in width with all boundaries free-slip. A 40-km thick "sticky air" layer (with zero density, $10^{19}Pa \cdot s$ viscosity) is included on the top. The lithospheric thickness of the proto-continent is the same as that of the ocean. We use 320×1280 elements (40 particles per element) to resolve the model domain. The horizontal resolution is 2.5 km and the vertical resolution gradually increases from 2.5 km at the bottom to 1 km at the top of 60 km. A case with a higher resolution (1 km \times 1 km throughout) is also used with no influence on the outcomes. The transitional area (from x=1000 km to 1100 km in Fig. 2A) between proto-continent and oceanic domain is a circle arc tangent to the

crustal surface. The strength of the proto-continental margin is determined by the maximum yield stress τ_{max} (150-600 MPa) and the lithospheric thickness (100-150 km) (Figs. 3A-B). For the reference model, the maximum yield stress of the lithosphere is 300 MPa and the friction coefficient of sediment is 0.05. Other parameters are listed in Table S1.

Depositional settings and the critical sediment thickness

We developed an ocean-mixing model to determine the spatial distribution of the depositional rate $v_d(x)$. In the model, photoferrotrophic bacteria need to acquire the nutrients transported away from the proto-continental margin (with an eddy-diffusion model) and produce BIF sediments. Their accumulation causes the localization of BIF deposition on the edge of the proto-continent. The depositional rate, v_d , changes in proportion to the nutrient concentration, c. For the oceans, a one-dimensional half space is assumed with distance x from the ocean-continent boundary (x = 0) to the open ocean ($x = +\infty$). At the ocean-continent boundary (x = 0), we set a fixed nutrient flux f_0 from the proto-continent and a zero concentration in the far-field. The 1-D diffusion-reaction equation is solved for the nutrient concentration, c(x)

$$\kappa_D \frac{d^2 c(x)}{dx^2} - g(x) = 0 \tag{12}$$

where κ_D is the eddy diffusivity and g(x) is the reaction term (i.e., nutrient consumption by bacteria). With a constant reaction rate m:

$$g(x) = mc(x) \tag{13}$$

eq. 12 and the boundary conditions become:

$$\frac{d^{2}c(x)}{dx^{2}} - \frac{m}{\kappa_{D}}c(x) = 0$$

$$\frac{dc}{dx}|_{x=0} = -\frac{f_{0}}{\kappa_{D}}, c|_{x=+\infty} = 0$$
(14)

545 The normalized solution is

$$v_d(x) = c(x) = e^{-\frac{3}{d_0}x} \tag{15}$$

- where $d_0 = 3\sqrt{\frac{\kappa_D}{m}}$, the width of the depositional region $(v_d|_{x=d_0} = 5\%)$.
- Since direct observations of the nutrient spatial distribution on the modern
- 549 continental margin are rare, the concentration of the photosynthetic bacteria is
- 550 represented by chlorophyll-a concentration (Fig. S4B). Twenty profiles across
- continental margins are selected, and they are well fit with the 1-D analytical solution
- 552 (the fitting results of two typical profiles are shown in Fig. S4C). The range of the d_0
- of these profiles varies from 71 km to 293 km.
- With a specific deposition rate $v_d(x)$, over a time Δt , BIF sediment of thickness,
- h(x), is placed on top of the solid surface replacing the sticky-air material:

$$h(x) = v_d(x)\Delta t, \tag{16}$$

- We set Δt to 1 Myr in most cases. Smaller values of Δt were tested, but they did not
- substantially change the results (Fig. S3E).
- We also defined the critical thickness to represent the minimum sediment thickness
- required to break the continental margin. We stop adding BIFs into the model once the
- continental margin begins to collapse. If the horizontally averaged thickness of the BIFs
- at this time is h_{ave} , the critical thickness h_c is also recorded as h_{ave} .

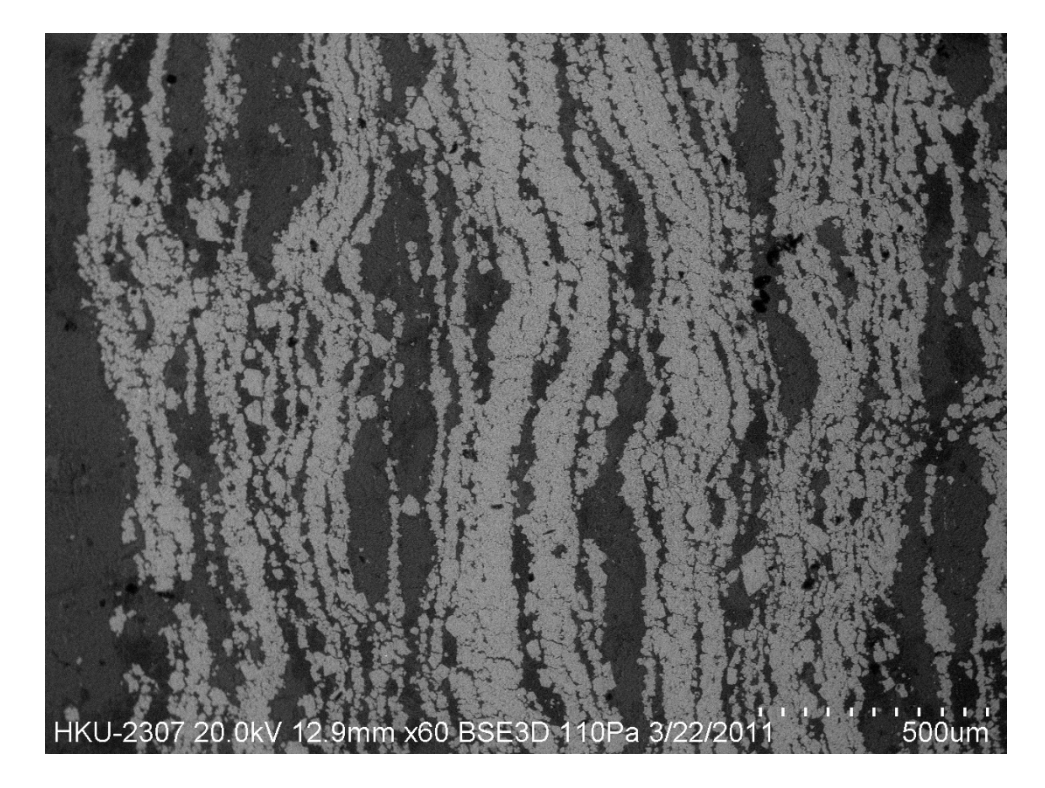


Figure S1 | The scanning electron microscope (SEM) observation of the magnetiterich BIF from Dales Gorge in 2.47 Ga (19). The dark part is mainly quartz and the grey part is magnetite, the average density is \sim 4.2 g/cm³.

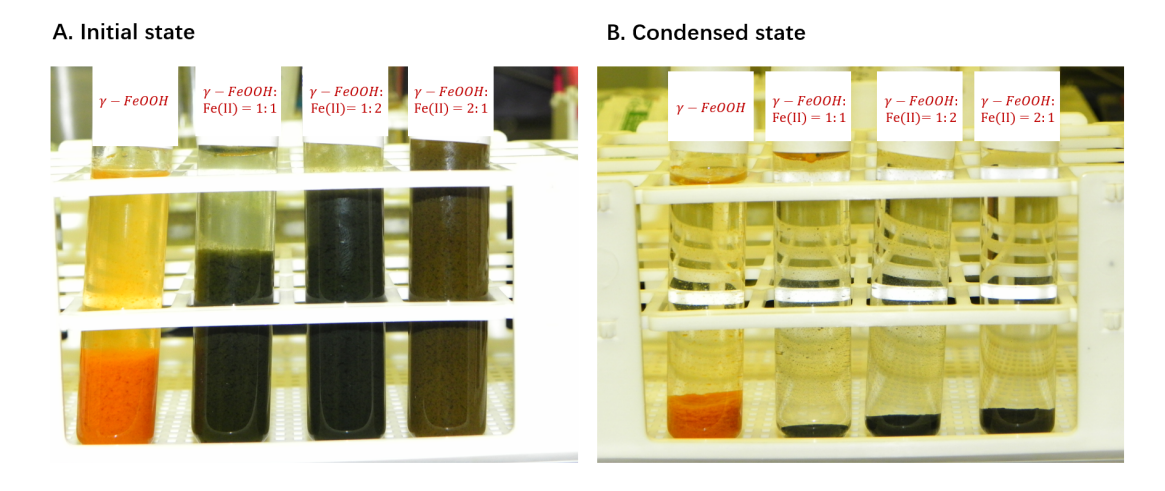


Figure S2 | The formation of dense magnetite by the reaction between Fe(II) and the fluffy $\gamma - FeOOH$ (lepidocrocite). A. From left to right showing the initial state

of (1) the slurry only containing $\gamma - FeOOH$; (2) the slurry containing $\gamma - FeOOH$ and Fe(II) in the ratio of 1:1 (green rust); (3) the slurry containing $\gamma - FeOOH$ and Fe(II) in the ratio of 1:2 (green rust); (4) the slurry containing $\gamma - FeOOH$ and Fe(II) in the ratio of 2:1 (green rust). **B.** The corresponding condensed state of the iron oxides after the green rust turned to magnetite via the dissolution-recrystallization process. The tubes amended with Fe(II) formed the denser black magnetite, compared with the still fluffy $\gamma - FeOOH$ slurry without the amendment of Fe(II).

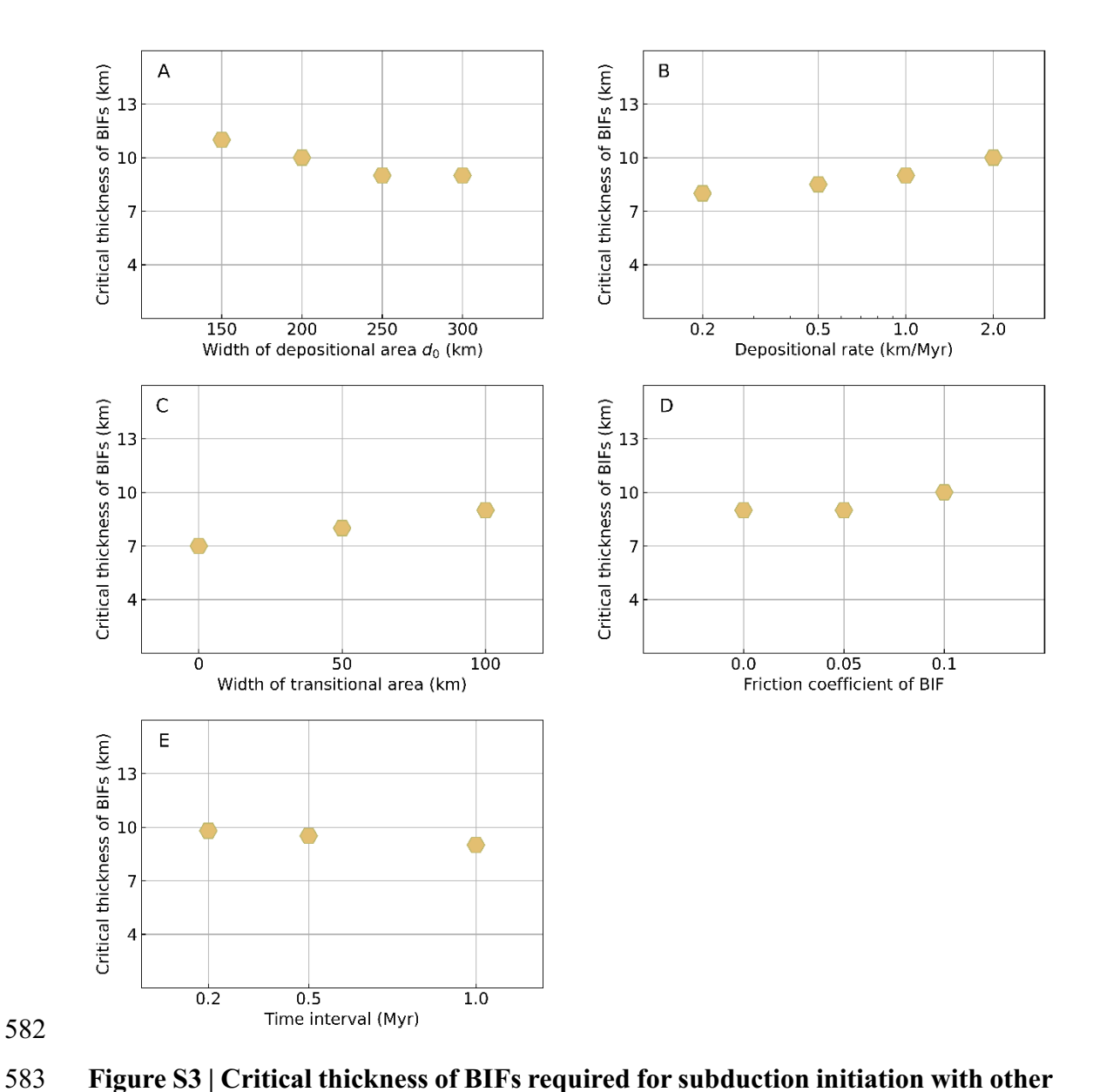


Figure S3 | Critical thickness of BIFs required for subduction initiation with other insignificant parameters: A. Width of the depositional area. B. BIF depositional rate.
C. Width of transitional area between the proto-continent and oceanic plate. D. Friction coefficient of BIF sediments. E. Time interval to deposit BIFs.

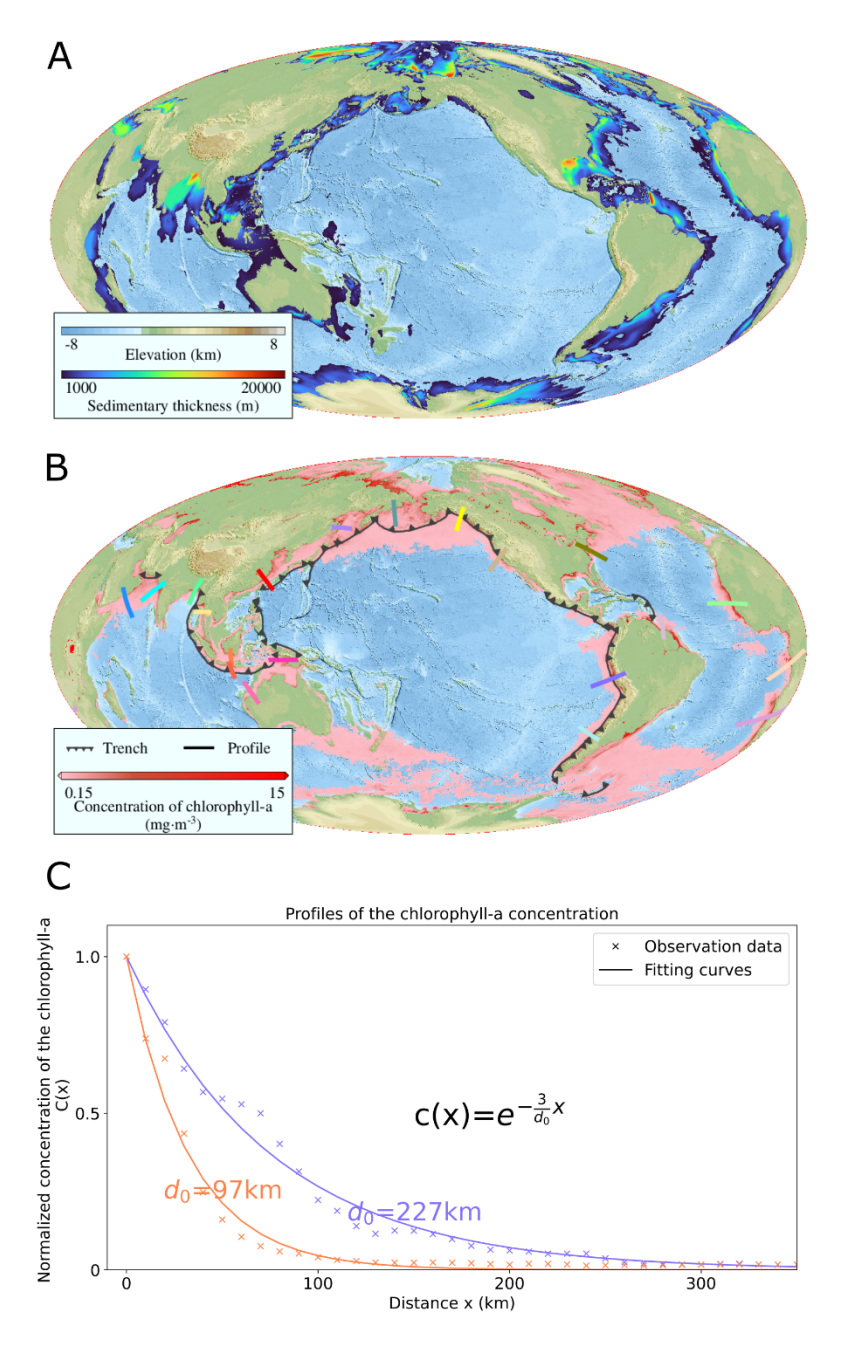


Figure S4 | The overlap of the biological photic zones and the subduction zones on modern continental margins, as the analog to the Neoarchean continental margins.

A. Distribution of the sedimentary thickness on modern continental margins. B. Distribution of the photosynthetic intensity and the subduction boundaries near the modern continental margins. The chlorophyll-a is an important photosynthetic pigment

and its concentration can reflect the intensity of photosynthesis (49). Areas with concentrations larger than $0.15~{\rm mg\cdot m^{-3}}$ are filled with the pink-red color. This figure shows the modern photic zones with the highest primary productivity are mainly distributed on continental margins. **C.** The typical profiles of the normalized chlorophyll-a concentration and their fitting results. Their position can be found in B with the corresponding color.

Table S1 | Model constants.

Material	reference density $(g \cdot cm^{-3})$	coefficient of thermal expansion $\alpha(K^{-1})$	specific heat capacity C_p $(J \cdot kg^{-1} \cdot K^{-1})$	thermal diffusivity $\kappa (m^2 \cdot s^{-1})$	shear modulus K_e (GPa)	dislocation creep parameters	diffusion creep parameters	plasticity parameters
Air	0.00	3×10^{-5}	1000	1×10^{-3}	-	$\eta = 10^{19} Pa \cdot s$	-	-
BIF sediment	3.80-4.60	3×10^{-5}	1000	1×10^{-6}	-	$\eta_0 = 4.1 \times 10^{17} Pa \cdot s,$ n = 2.3, $E = 154 kJ \cdot mol^{-1},$ $V = 8J \cdot MPa^{-1} \cdot mol^{-1}$	-	$\mu = 0.0 \text{-} 0.1,$ $C_0 = 10 MPa,$ $C_f = 1MPa$
Continental crust	2.90	3×10^{-5}	1000	1×10^{-6}	30	$\begin{split} &\eta_0 = 4.1 \times 10^{17} Pa \cdot s, \\ &n = 2.3, \\ &E = 154 kJ \cdot mol^{-1}, \\ &V = 8J \cdot MPa^{-1} \cdot mol^{-1} \end{split}$	-	$\begin{array}{c} \mu = 0.1 {\sim} 0.4, \\ C_0 = 10 \; MPa, \\ C_f = 1 MPa, \\ \tau_{max} = 150 {\sim} 600 \; MPa \end{array}$
Continental lithospheric mantle	3.25	3×10^{-5}	1000	1×10^{-6}	30	$\begin{array}{l} \eta_0 = 2.0 \times 10^{19} Pa \cdot s, \\ n = 3.5, \\ E = 540 kJ \cdot mol^{-1}, \\ V = 13 J \cdot MPa^{-1} \cdot mol^{-1} \end{array}$	$\begin{array}{l} \eta_0 = 1.0 \times 10^{19} \ Pa \cdot s, \\ n = 1.0, \\ E = 300 \ kJ \cdot mol^{-1}, \\ V = 4J \cdot MPa^{-1} \cdot mol^{-1} \end{array}$	$\begin{array}{c} \mu = 0.1 {\sim} 0.4, \\ C_0 = 10 \ MPa, \\ C_f = 1 MPa, \\ \tau_{max} = 150 {\sim} 600 \ MPa \end{array}$
Oceanic crust	3.00	3×10^{-5}	1000	1×10^{-6}	30	$\begin{split} &\eta_0 = 4.1 \times 10^{17} Pa \cdot s, \\ &n = 2.3, \\ &E = 154 kJ \cdot mol^{-1}, \\ &V = 8J \cdot MPa^{-1} \cdot mol^{-1} \end{split}$	-	$\mu = 0.1 \sim 0.4,$ $C_0 = 10 MPa,$ $C_f = 1MPa,$ $\tau_{max} = 50 MPa$
Oceanic lithospheric mantle	3.30	3×10^{-5}	1000	1×10^{-6}	30	$\begin{array}{l} \eta_0 = 2.0 \times 10^{19} \ Pa \cdot s, \\ n = 3.5, \\ E = 540 \ kJ \cdot mol^{-1}, \\ V = 13 \ J \cdot MPa^{-1} \cdot mol^{-1} \end{array}$	$\begin{array}{l} \eta_0 = 1.0 \times 10^{19} Pa \cdot s, \\ n = 1.0, \\ E = 300 kJ \cdot mol^{-1}, \\ V = 4J \cdot MPa^{-1} \cdot mol^{-1} \end{array}$	$\begin{array}{c} \mu = 0.1{\sim}0.4, \\ C_0 = 10 MPa, \\ C_f = 1MPa, \\ \tau_{max} = 150{\sim}600 MPa \end{array}$
Asthenospheric mantle	3.30	3×10^{-5}	1000	1×10^{-6}	30	$\eta_0 = 2.0 \times 10^{19} Pa \cdot s,$ n = 3.5, $E = 540 kJ \cdot mol^{-1},$ $V = 13 J \cdot MPa^{-1} \cdot mol^{-1}$	$\begin{split} \eta_0 &= 1.0 \times 10^{19} Pa \cdot s, \\ n &= 1.0, \\ E &= 300 kJ \cdot mol^{-1}, \\ V &= 4J \cdot MPa^{-1} \cdot mol^{-1} \end{split}$	$\begin{array}{l} \mu = 0.1{\sim}0.4, \\ C_0 = 10MPa, \\ C_f = 1MPa, \\ \tau_{max} = 150{\sim}600MPa \end{array}$